

# Texture inhomogeneity in a Ti–Nb-based $\beta$ -titanium alloy after warm rolling and recrystallization

B. Sander, D. Raabe\*

Max-Planck-Institut für Eisenforschung, Max-Planck-Str. 1, 40237 Düsseldorf, Germany

Received 1 May 2007; received in revised form 15 June 2007; accepted 18 June 2007

## Abstract

The crystallographic microtexture and microstructure of a  $\beta$ -titanium alloy (Ti–35 wt.% Nb–7 wt.% Zr–5 wt.% Ta) is studied after warm rolling and recrystallization. The main observations are the evolution of partially recrystallized microstructures during warm rolling and the formation of strong through-thickness texture and microstructure gradients at larger strains. Both, the recrystallized volume fraction and the texture depend on the thickness reduction. At small reductions ( $\leq 50\%$ ) texture gradients are also small showing some  $\alpha_{\text{bcc}}$ -fiber (crystallographic axis  $\langle 1\ 1\ 0 \rangle$  parallel to the rolling direction) and  $\gamma$ -fiber (crystallographic axis  $\langle 1\ 1\ 1 \rangle$  parallel to the normal direction) texture components. At larger strains (70–90%) the texture and microstructure gradients are characterized by shear texture components and dynamic recrystallization particularly close to the surface layers and plane strain texture components which are typical of recovered grains in the center layer.  
© 2007 Elsevier B.V. All rights reserved.

**Keywords:** Texture; Rolling; Biomaterial; Titanium; Crystal plasticity; Goss; Recrystallization; Recovery; Shear texture

## 1. Introduction

Ti-base alloys occur in one or a mixture of two basic crystalline structures, namely, the hexagonal  $\alpha$ -phase and body-centered cubic (bcc)  $\beta$ -phase. Ti-based alloys generally fall in either of the three main groups of  $\alpha$ -,  $\alpha + \beta$ - and  $\beta$ -type alloys [1]. The transition temperature from the  $\alpha$  to the  $\beta$ -phase is 882 °C for pure Ti. Elements which promote higher or lower transformation temperatures are referred to as  $\alpha$  stabilizers (like O, Al, La) or  $\beta$  stabilizers (like Mo, V, Nb, Ta, Fe), respectively [1].

This investigation is about a novel quaternary  $\beta$ -alloy, namely, on Ti–35 wt.% Nb–7 wt.% Zr–5 wt.% Ta [2], with the aim to study the evolution of the crystallographic texture during warm rolling and subsequent static recrystallization.

The study of crystallographic textures in single phase  $\beta$ -alloys or in the  $\beta$ -phase of dual phase alloys is of relevance for better understanding a variety of metallurgical mechanisms and mechanical properties in such alloys. For instance, the understanding of  $\beta$ -phase Ti textures is relevant for the

investigation of the active slip systems; the crystallography of the  $\alpha \rightarrow \beta \rightarrow \alpha$  phase transformation mechanisms; the overall mechanical anisotropy of textured material; fatigue; creep; forming (conventional and superplastic) and the elastic anisotropy in the context of biomedical alloy grades. These aspects apply to both single phase and dual phase alloys [3–25].

Our particular interest in the evolution of texture in the current single phase  $\beta$  Ti–35 wt.% Nb–7 wt.% Zr–5 wt.% Ta alloy focuses on the aspect of texture inhomogeneity. Specifically, we examine the formation of through-thickness texture gradients that were created during warm rolling, which are partly inherited in the subsequent recrystallization processes. Deformation-induced through-thickness texture inhomogeneity is a well known phenomenon in warm rolled polycrystalline materials [26–32]. This applies in particular to bcc metals since they have a strong tendency to undergo pronounced orientation-dependent recovery (particularly in the 45° normal rotated cube component  $[0\ 0\ 1]\langle 1\ 1\ 0 \rangle$ ). Recovery competes strongly with primary recrystallization [33–36]. This difference (between recrystallization and recovery) is important in the field of texture analysis because recovery preserves the deformation texture, while recrystallization changes it. Also, different through-thickness deformation texture layers in warm rolled bcc polycrystals lead to corresponding differences in the local recrystallization behavior.

\* Corresponding author.  
E-mail addresses: b.sander@mpie.de (B. Sander),  
d.raabe@mpie.de (D. Raabe).

Understanding the origins of these orientation and process-dependent texture inhomogeneities in warm rolled sheets is a necessary step towards optimization of microstructure-based processes to achieve better texture homogeneity in such alloys.

## 2. Experimental methods

### 2.1. Metallurgy

The  $\beta$ -phase Ti–35 wt.% Nb–7 wt.% Zr–5 wt.% Ta alloy (hereafter abbreviated 35-7-5) was melted in an electric arc furnace. All of the elements used in the alloy had a high purity (Table 1). The electric arc furnace was evacuated and subsequently flooded with Argon at a pressure of 300 mbar. The furnace was equipped with a water cooled copper crucible. The temperature of the electric arc was about 3000 °C while the melt was at the center hold at a peak temperature of 1830–1850 °C in order to assure complete dissolution of the Nb, Ta or Mo, respectively. The electric arc method provided an intense stirring effect. Melting all ingredients required about 30–60 s. In order to obtain cast samples of optimal chemical and structural homogeneity all specimens were remelted several times. Each sample was stirred completely after remelting in the crucible, and then turned about its horizontal axis by use of an in-furnace manipulator, and subsequently reheated above the melting point. This procedure (melting, stirring, solidification, rotation) was repeated four times. After the fourth remelting, the sample was cast into a rectangular copper mold which had a size of 60 mm  $\times$  32.6 mm  $\times$  10 mm. The copper mold had a temperature of about 30 °C which led to rapid solidification entailing only microsegregation and suppressing dendrite formation.

### 2.2. Homogenization, rolling and recrystallization processing

The as-cast samples were solution heat treated at 1473 K (1200 °C) for 4 h in order to homogenize the sample and remove microsegregation. Since Ti alloys undergo very strong chemical reactions with oxygen the sample was heat treated under a high purity Argon atmosphere.

Reversing warm rolling was conducted immediately after pre-heating at a temperature of 850 °C for 15 min. Rolling was performed on a two-high stand. The pre-heating procedure was repeated after each rolling step, leading to the possibility for recrystallization between the warm rolling steps. The maximum reduction was 90% engineering sheet thickness reduction. Samples for detailed investigation were cut after 20, 50, 70 and 90% rolling reduction. The separate rolling steps yielded about 10%

reduction per step. Using larger reductions per step could lead to edge cracking. The maximum rolling force was 600 kN. The diameter of the working rolls was 190 mm. The final recrystallization treatment of the 90% rolled specimen was conducted at 900 °C for 45 min.

### 2.3. Characterization methods

Characterization of the chemical and microstructural homogeneity of the cast and heat treated samples was conducted using optical and scanning electron microscopy (SEM) in conjunction with energy dispersive X-ray spectrometry (EDX) and electron back scatter diffraction (EBSD).

Grinding before microscopy was performed using 400, 600, 1200 and 2400 paper with subsequent use of 6  $\mu$ m (45 min), 3  $\mu$ m (20 min) and 1  $\mu$ m (15 min) polishing. For optical microscopy the samples were etched using a solution of 68 ml glycerin, 16 ml HNO<sub>3</sub> and 16 ml Hf. For SEM observations the specimens were electropolished for 60 s at 35 V after the 1  $\mu$ m polishing step.

The elastic properties were measured using an ultrasonic resonance frequency method (Grindo-Sonic). This method measures the elastic modulus by analyzing the natural period of the transient vibration which results from a mechanical disturbance of the object tested. The Grindo-Sonic device transforms the incoming signal received from this natural frequency in an electric current of the same frequency and relative amplitude, during eight periods, due to a quartz clock where a reference crystal oscillates at a given frequency.

In order to measure the volume fractions of the two phases after thermal homogenization X-ray wide angle Bragg diffraction experiments were used with CoK $\alpha$ 1 radiation obtained from a tube operated at 40 mA, 40 kV.

## 3. Basics on warm rolling textures of bcc metals without phase transformation

According to the cubic crystal symmetry of the  $\beta$ -Ti lattice structure and the nearly orthotropic symmetry of the hot rolled specimens (RD, rolling direction; ND, normal direction and TD, transverse direction) the crystallographic textures are typically presented in the reduced Euler space ( $0^\circ \leq \varphi_1, \phi, \varphi_2 \leq 90^\circ$ ). Since warm rolled bcc polycrystals tend to develop pronounced texture fibers during rolling, it is convenient to present  $\varphi_1$ -sections through Euler space or to present the orientation density along various characteristic orientation fibers. The most relevant texture fibers for warm rolled bcc metals are the  $\alpha_{\text{bcc}}$ -fiber (crystallographic fiber axis  $\langle 110 \rangle$  parallel to the rolling direction including major components  $\{001\}\langle 110 \rangle$ ,  $\{112\}\langle 110 \rangle$  and  $\{111\}\langle 110 \rangle$ ),  $\gamma$ -fiber (crystallographic fiber axis  $\langle 111 \rangle$  parallel to the normal direction including major components  $\{111\}\langle 110 \rangle$  and  $\{111\}\langle 112 \rangle$ ),  $\eta$ -fiber (crystallographic fiber axis  $\langle 001 \rangle$  parallel to the rolling direction including major components  $\{001\}\langle 100 \rangle$  and  $\{011\}\langle 100 \rangle$ ),  $\zeta$ -fiber (crystallographic fiber axis  $\langle 011 \rangle$  parallel to the normal direction including major components  $\{011\}\langle 100 \rangle$ ,  $\{011\}\langle 211 \rangle$ ,  $\{011\}\langle 111 \rangle$  and  $\{011\}\langle 011 \rangle$ ),  $\varepsilon$ -fiber (crys-

Table 1  
Alloy composition

	Ti	Nb	Zr	Ta
wt.%	53	35	7	5
at.%	69.7	23.7	4.8	1.7

Table 2  
Some important fibers and texture components for crystallographic textures of bcc alloys (RD, rolling direction; ND, normal direction and TD, transverse direction) [28,30,32,36]

Material	Fiber name	Fiber axis	Important texture components
bcc metal	$\alpha_{\text{bcc}}$ -fiber	$\langle 110 \rangle$ parallel to RD	$\{001\}\langle 110 \rangle$ , $\{112\}\langle 110 \rangle$ , $\{111\}\langle 110 \rangle$
	$\gamma$ -fiber	$\langle 111 \rangle$ parallel to ND	$\{111\}\langle 110 \rangle$ , $\{111\}\langle 112 \rangle$
	$\eta$ -fiber	$\langle 001 \rangle$ parallel to RD	$\{001\}\langle 100 \rangle$ , $\{011\}\langle 100 \rangle$
	$\zeta$ -fiber	$\langle 011 \rangle$ parallel to ND	$\{011\}\langle 100 \rangle$ , $\{011\}\langle 211 \rangle$ , $\{011\}\langle 111 \rangle$ , $\{011\}\langle 011 \rangle$
	$\varepsilon$ -fiber	$\langle 011 \rangle$ parallel to TD	$\{001\}\langle 110 \rangle$ , $\{112\}\langle 111 \rangle$
	$\theta$ -fiber	$\langle 001 \rangle$ parallel to ND	$\{441\}\langle 11118 \rangle$ , $\{111\}\langle 112 \rangle$ , $\{11118\}\langle 4411 \rangle$ , $\{011\}\langle 100 \rangle$
	$\beta_{\text{bcc}}$ -skeleton line	$\approx \langle 111 \rangle$ close to ND	$\{001\}\langle 100 \rangle$ , $\{001\}\langle 110 \rangle$ $\{111\}\langle 110 \rangle$ , $\{557\}\langle 583 \rangle$ , $\{111\}\langle 112 \rangle$

tallographic fiber axis  $\langle 011 \rangle$  parallel to the transverse direction including major components  $\{001\}\langle 110 \rangle$ ,  $\{112\}\langle 111 \rangle$ ,  $\{111\}\langle 112 \rangle$  and  $\{011\}\langle 100 \rangle$  and  $\theta$ -fiber (crystallographic fiber axis  $\langle 001 \rangle$  parallel to the normal direction including major components  $\{001\}\langle 100 \rangle$  and  $\{001\}\langle 110 \rangle$ ). The most important orientations and fibers are given in Table 2 [26–37].

#### 4. Experimental results

##### 4.1. Metallurgical results, homogenization treatment and mechanical data

Fig. 1 shows that the microstructure and microtexture of the as-cast alloy Ti–35 wt.% Nb–7 wt.% Zr–5 wt.% Ta in three perpendicular sections. The EBSD maps reveal that the texture and grain structure of the as-cast material is practically random and that the grains have a nearly globular (equiaxed) grain shape.

Figs. 2 and 3 show that the specimen revealed pronounced microsegregation in the as-cast state which was removed by a corresponding homogenization heat treatment at 1473 K (1200 °C) under Argon atmosphere for 4 h.

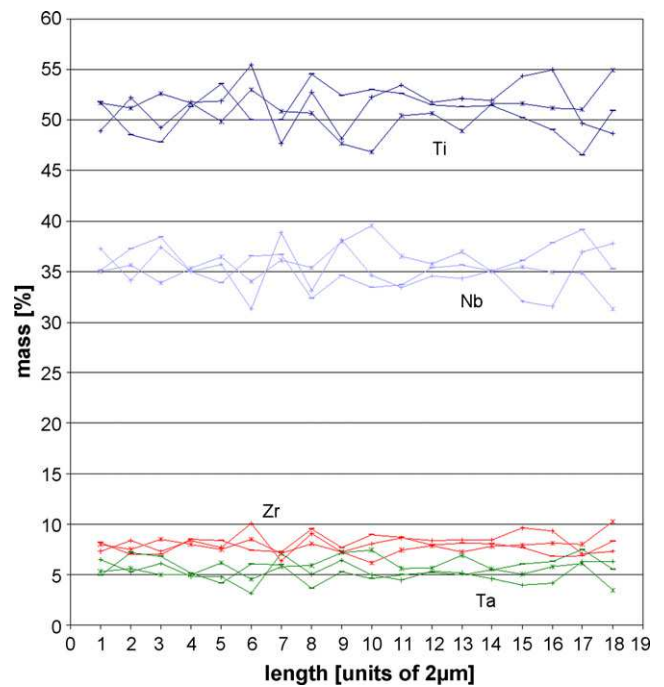


Fig. 2. EDX line scans before the heat treatment, alloy 35-7-5.

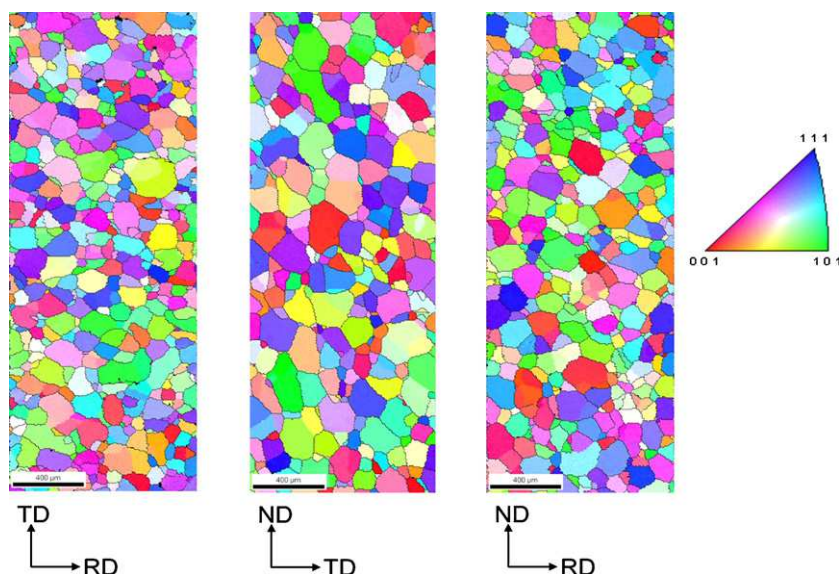


Fig. 1. EBSD inverse pole figure orientation maps of the as cast 35-7-5 alloy show nearly random texture and globular (equiaxed) grains. Maps are presented with respect to the sample coordinate system for subsequent rolling; microstructure from three perpendicular sections referenced to the normal direction (ND); RD and TD refer to subsequent longitudinal and transverse directions.

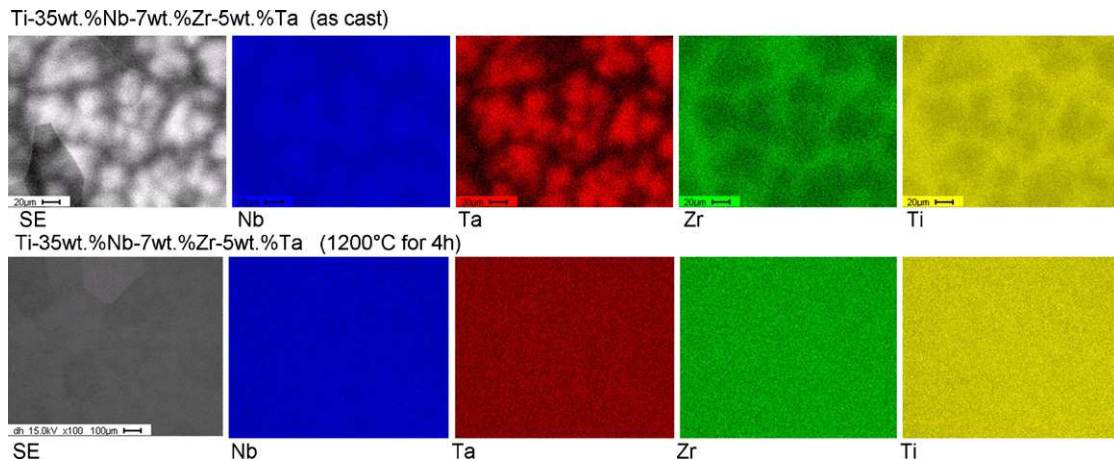


Fig. 3. EDX area analysis before and after the heat treatment, alloy 35-7-5.

The X-ray diffraction scan presented in Fig. 4, taken after the heat treatment, shows that the material consisted essentially of the bcc  $\beta$ -phase before warm rolling. The volume fractions of the  $\alpha$ - and  $\omega$ -phases are negligible.

The ultrasonic measurement of the elastic properties revealed that the bulk polycrystal modulus of the heat treated Ti–35 wt.% Nb–7 wt.% Zr–5 wt.% Ta alloy was as low as 59.9 GPa (the pure hexagonal Ti reference sample had a modulus of 114.7 GPa). Fig. 5 shows the flow curve for the material taken under compressive load. The test was conducted with a cylindrical sample (1 cm diameter) after casting and homogenization at a strain rate of  $0.01 \text{ s}^{-1}$  using lubrication. The compression axis was parallel to the normal direction of the cast (and later warm rolled) sample.

#### 4.2. Optical metallography of rolled specimens

Fig. 6 shows the optical metallography from longitudinal sections of the warm rolled samples at different strains. The 20 and 50% rolled specimens reveal the formation of microbands. After 70 and 90% thickness reduction partially recrystallized zones become visible. In the 70% rolled sample layers of new small grains appear as necklace structures along the former grain boundaries surrounding the deformed grains. The 90% rolled sample reveals both fully recrystallized zones and also some

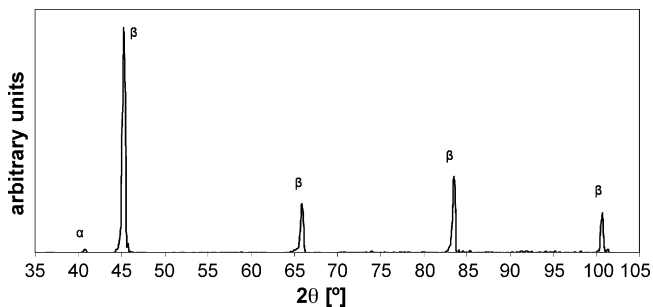


Fig. 4. X-ray Bragg diffraction scan of the 35-7-5 alloy after heat treatment ( $\text{CoK}\alpha_1$  radiation, 40 mA, 40 kV). The intensity is given in arbitrary units as function of the diffraction angle  $2\theta$ . The data reveal that the specimen consists essentially of the  $\beta$ -phase.

very long as-deformed grains which do not contain recrystallized crystals.

#### 4.3. Microtexture of rolled and annealed specimens

Fig. 7 shows microtexture maps of the rolled samples; ND  $\{hkl\}$  and RD  $\langle uvw \rangle$ , image quality, and Kernel average for the 20% (a), 50% (b), 70% (c) and 90% (d) warm rolled ( $850^\circ\text{C}$ ) samples in longitudinal sections from the entire thickness (top to bottom surface). The ND and RD EBSD maps jointly allow one to identify all orientations in terms of the crystal directions in the normal  $\{hkl\}$  and of the lattice rolling direction  $\langle uvw \rangle$  at each point relative to the macroscopic sample coordinates. The image quality map provides a qualitative measure of the local lattice distortion and the Kernel average misorientation is a measure of the local lattice orientation gradients in the vicinity of a given coordinate. The latter quantity is of particular help for discriminating recrystallized from non-recrystallized material.

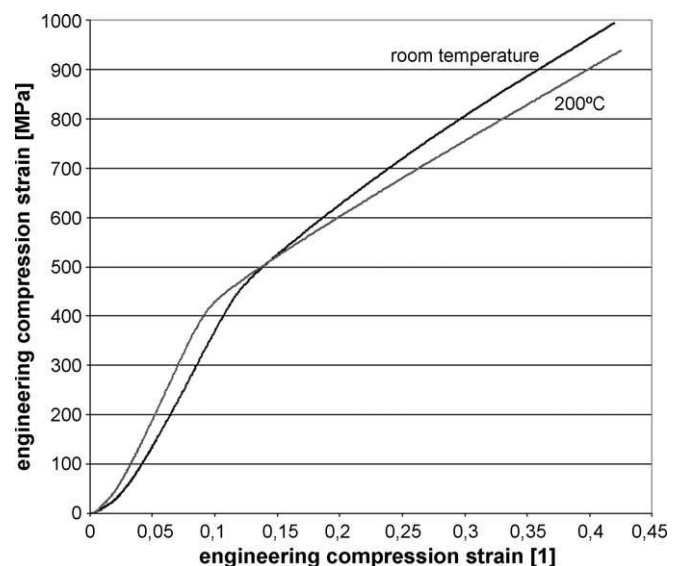


Fig. 5. Flow curves obtained from compression testing; cylindrical sample (1 cm diameter); after casting and homogenization; strain rate  $0.01 \text{ s}^{-1}$ ; lubrication; compression axis along ND.

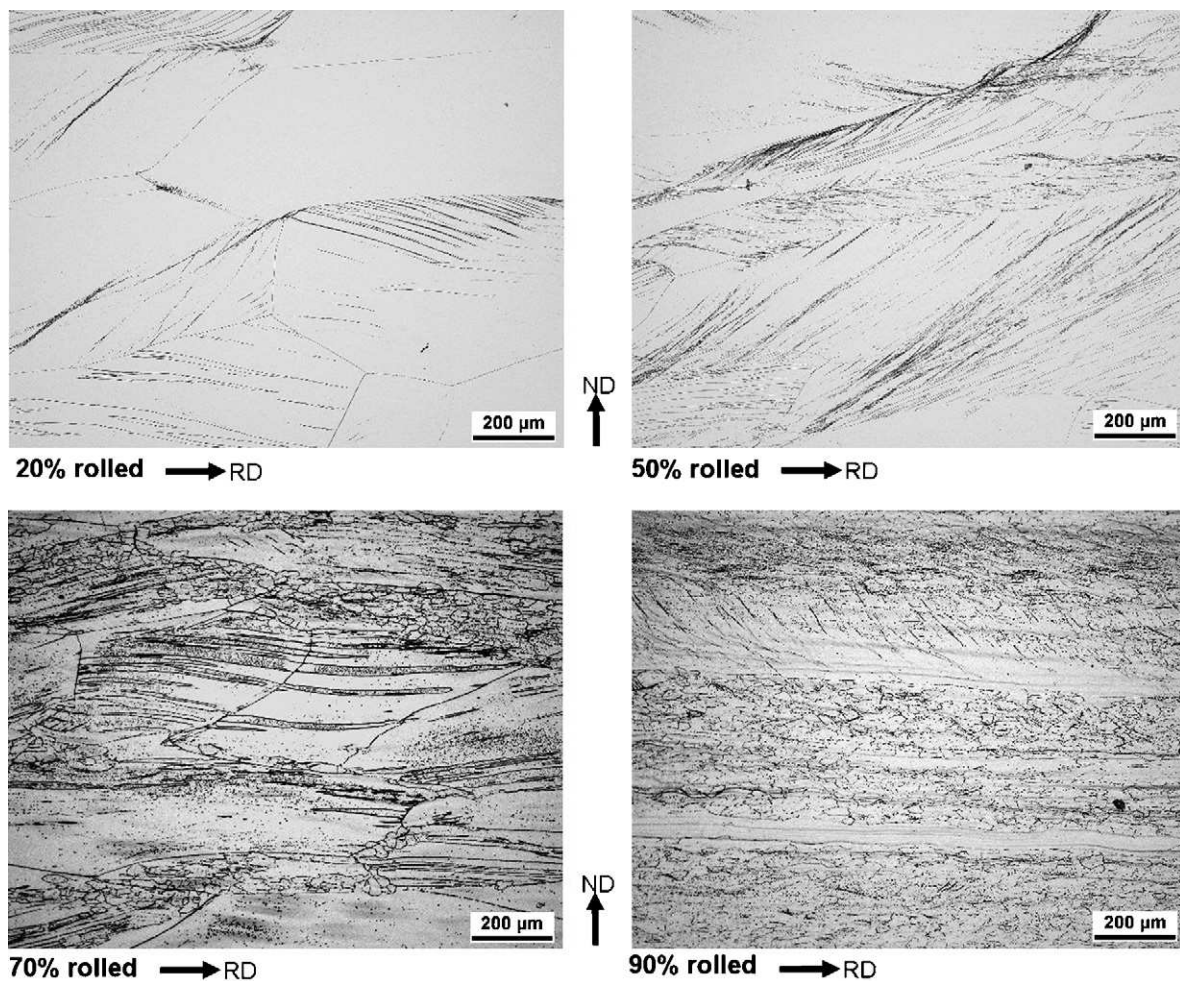


Fig. 6. Optical metallography (longitudinal sections) of warm rolled (850 °C) samples after different thickness reductions.

Blue areas (minimum value of the Kernel average misorientation) indicate freshly recrystallized material.

After 20% rolling reduction the EBSD maps (Fig. 7a) and the corresponding orientation distribution function (ODF) (Fig. 8a) reveal a dominant  $\{111\}$  (blue)  $\langle 110 \rangle$  (green) orientation. The in-grain deformation structure is inhomogeneously distributed after 20% reduction. While some crystals exhibit a pronounced in-grain deformation pattern, others appear only weakly strained.

After 50% rolling reduction, Figs. 7b and 8b reveal a dominant  $\{111\}$   $\langle 110 \rangle$  orientation together with a gradually developing  $\alpha_{\text{bcc}}$ -fiber ( $\langle 110 \rangle$  parallel to RD; see Table 2). The strongest component on the  $\alpha_{\text{bcc}}$ -fiber is an orientation close to  $\{112\}\langle 110 \rangle$ . Close to the  $\gamma$ -fiber ( $\langle 111 \rangle$  parallel to ND; see Table 2) a strong  $\{554\}\langle 225 \rangle$  texture component develops. The Kernel average map in Fig. 7b shows that some of the larger grains reveal only small local orientation scatter in their grain interior. Stronger orientation gradients clearly prevail at the grain boundaries. Some grains reveal strong shear bands with pronounced orientation gradients with respect to the surrounding matrix orientations.

After 70% rolling reduction Fig. 7c shows the beginning of recrystallization. The formation of new grains is very hetero-

geneously distributed in the microstructure. In some grains no recrystallized crystals occur at all (white arrows) while others appear fully transformed by recrystallization (black arrows). In some other grains recrystallization seems to occur along the former microbands (yellow arrows). The texture (Fig. 8c) consists mainly of orientations on the  $\gamma$ -fiber ( $\langle 111 \rangle$  parallel to ND) with a stronger  $\{111\}\langle 112 \rangle$  and a weaker  $\{111\}\langle 110 \rangle$  orientation.

After 90% warm rolling reduction the microstructure reveals strong gradients through the sheet thickness (Fig. 7d). The upper and lower thirds (top and bottom surface regions) of the longitudinal section reveal a strongly recrystallized microstructure with only some portions in the as-deformed state. The center layer (about one-third of the volume in the longitudinal section) consists mostly of recovered grains with distorted shapes. The exact center layer consists of a large elongated grain. The recrystallized grains in the outer surface and sub-surface layers have Goss (white arrows),  $\{11118\}\langle 4411 \rangle$  or  $\{111\}\langle 112 \rangle$  orientation. The center layer consists essentially of  $\alpha$ -fiber texture components (Figs. 7d and 8d).

After the final heat treatment (900 °C, 45 min) of the 90% warm rolled sheet the microstructure (Fig. 9) a fully recrystallized and coarsened grain structure is revealed. The average grain size is 32  $\mu\text{m}$  but it shows a substantial gradient across

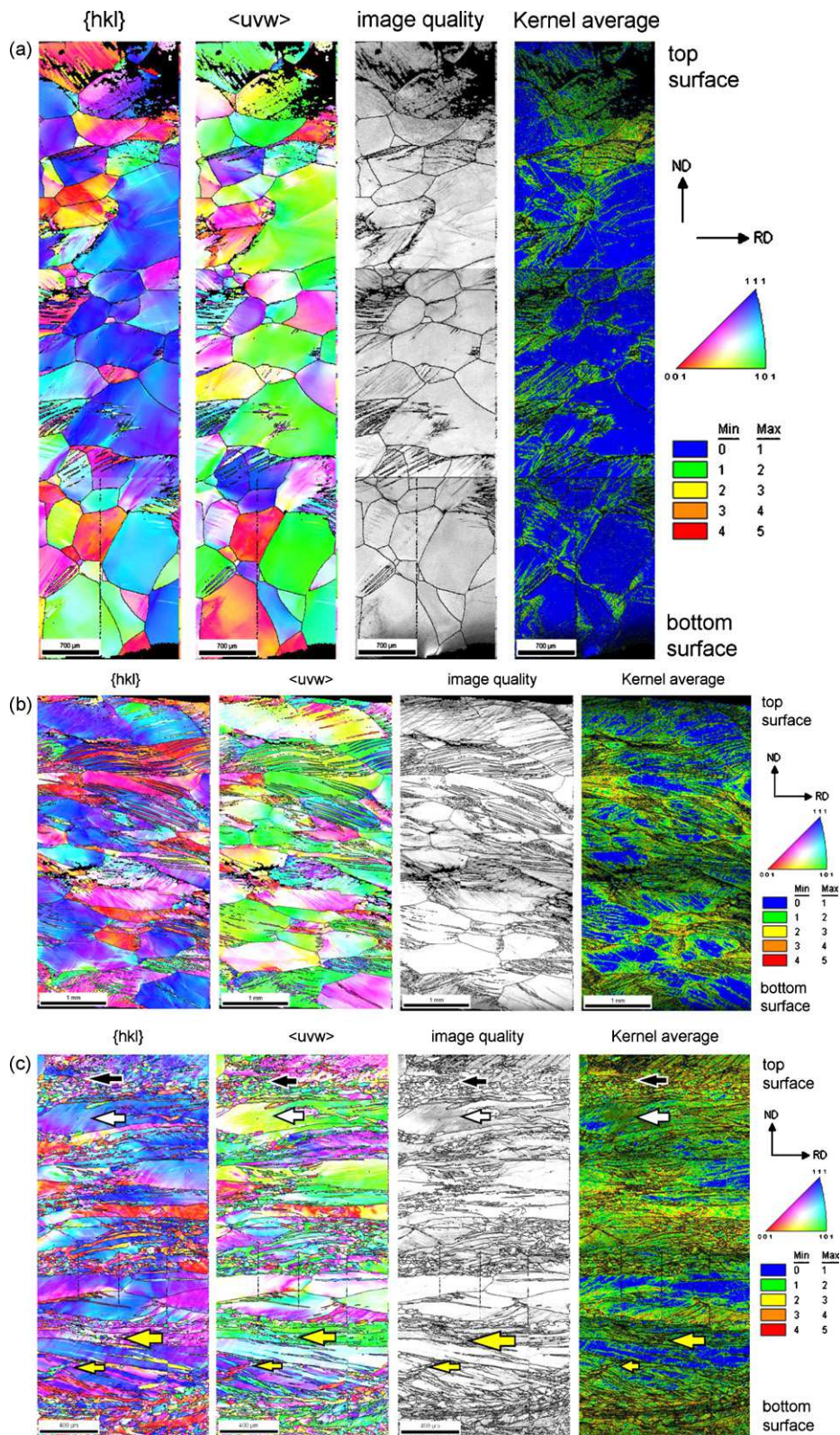


Fig. 7. (a–d) EBSD maps (ND  $\{hkl\}$  and RD  $\langle uvw \rangle$ ), image quality and Kernel average maps from 20, 50, 70 and 90% warm rolled (850 °C) samples in longitudinal sections from surface to surface.

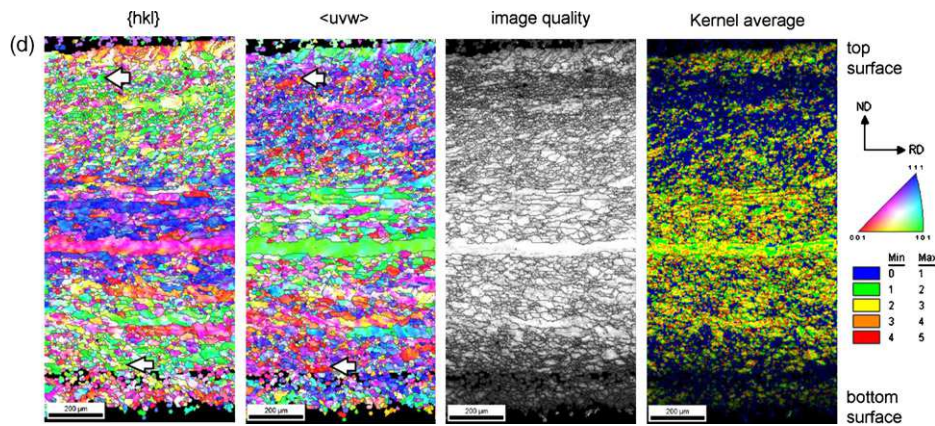


Fig. 7. (Continued).

the sheet thickness. The texture (Fig. 10) consists of a dominant  $\{111\}\langle 112\rangle$  texture component.

## 5. Discussion

### 5.1. Starting microstructure after casting and heat treatment

The X-ray and EDX results show that the alloy has a bcc lattice structure after the initial heat treatment. This is also confirmed by the EBSD results which is well suited to confirm the existence of second phases at  $\mu\text{m}$  scales since the back scattered electrons undergo Bragg diffraction and, therefore, different lattice structures can be discriminated. A disadvantage of the homogenization anneal is the grain coarsening that increases the grain size by a factor of about 5. For further optimization of this material it might, therefore, be a sensible strategy to first impose one or two strong warm reduction steps before conducting a homogenization heat treatment. Such a procedure might have two advantages. First, it might lead to grain refinement. Second, chemical homogenization could be faster and more efficient since the newly growing grains which sweep the material would introduce fast grain boundary diffusion as opposed to the slow volume diffusion. This procedure might entail more rapid removal of segregation effects.

For the subsequent warm rolling and heat treatment procedures it is very important that the initial grain structure is very homogeneous, randomly oriented, and nearly equiaxed (see Figs. 1 and 6), in order to promote recrystallization [30,33,36–40]. This high degree of microstructure and texture homogeneity before the further processing is attributed to the use of multiple solidification and re-melting steps and the rapid quench described above (see Section 2.1). The homogeneous starting conditions generally play an important role for texture evolution during subsequent processing of bcc materials since coarse grains and/or preferred casting textures usually entail strong inheritance effects. Microstructure (and texture) inheritance implies that certain preferred casting textures can lead to warm rolling microstructures which undergo strong recovery instead of recrystallization, particularly in bcc metals [30,33,36–42].

### 5.2. Microstructure and texture of warm rolled samples

At small and medium thickness reductions (up to 50%) no relevant recrystallized areas appear in the micrographs and EBSD maps. The texture evolution in this regime is characterized by the gradual evolution of an  $\alpha$ -fiber ( $\langle 110\rangle$  parallel to RD) and  $\gamma$ -fiber ( $\langle 111\rangle$  parallel to ND) texture: after 20% rolling reduction a dominant  $\{111\}\langle 110\rangle$  texture component exists. After 50% reduction an  $\alpha$ -fiber with a local texture maximum close to  $\{112\}\langle 110\rangle$  builds up. On the  $\gamma$ -fiber the  $\{111\}\langle 110\rangle$  orientation is accompanied by a  $\{111\}\langle 112\rangle$  component. These texture components are consistent with the crystallographic stability of these orientation at low and medium plane strains as, for instance, predicted by Taylor-type, self-consistent, and crystal plasticity finite element deformation models for bcc metals [40–51]. Pronounced shear-induced through-thickness gradients of the texture or of the grain morphology are not yet visible at this stage of deformation (below 50%). The texture observed at small and medium strains is comparable to that observed also for other warm rolled bcc metals and alloys which do not undergo phase transformation during warm rolling. For instance, due to their high Cr content 12–17% Cr alloyed ferritic stainless steels do not show much phase transformation during hot rolling so that they reveal similar textures as observed in this work for the bcc Ti alloy [28–36]. Similar observations apply for bcc refractory metals such as Mo and Ta [37–40]. Also Nb which is the major alloy element in the present case shows a similar texture evolution during rolling as observed for the current bcc Ti alloy [41].

After 70% thickness reduction the texture evolution is no longer dominated by the rolling deformation alone but it is also affected to a small extent by recrystallization processes. This is clearly visible from the EBSD map in Fig. 7c. The recrystallized material is characterized by three important features. First, the recrystallized grains are small and equiaxed. Second, they form a necklace-type morphology around the as-deformed grains. Third, the Kernel average map (Fig. 7c) reveals that the newly recrystallized crystals are not entirely free of in-grain orientation gradients but they seem to have been further deformed after the recrystallization step. These three observations suggest that the

recrystallization process might be a dynamic recrystallization mechanism.

The crystallographic texture after 70% thickness reduction shows a dominant  $\gamma$ -fiber with a strong maximum at the  $\{111\}\langle 112\rangle$  texture component. This transition from the  $\{111\}\langle 110\rangle$  to the  $\{111\}\langle 112\rangle$  orientation may be partially attributed to the recrystallization process (see microtexture maps in Fig. 7c) and partially to the increasing deformation. The intensity of the  $\alpha$ -fiber texture components has been reduced after 70% rolling reduction except for a remaining

local texture maximum on that fiber at  $\{001\}\langle 110\rangle$ . This effect differs from the texture evolution in rolled bcc alloys. As a rule, the  $\alpha$ -fiber texture components would gradually increase during rolling deformation [30–48]. In particular one would expect the  $\{112\}\langle 110\rangle$  orientation to occur as a rather strong plane strain deformation component after 70% thickness reduction as explained in a number of publications on stable deformation components in rolled bcc metals including pure Ta, Mo, Nb as well as highly alloyed stable ferritic stainless steels [37–52]. The fact that this prominent defor-

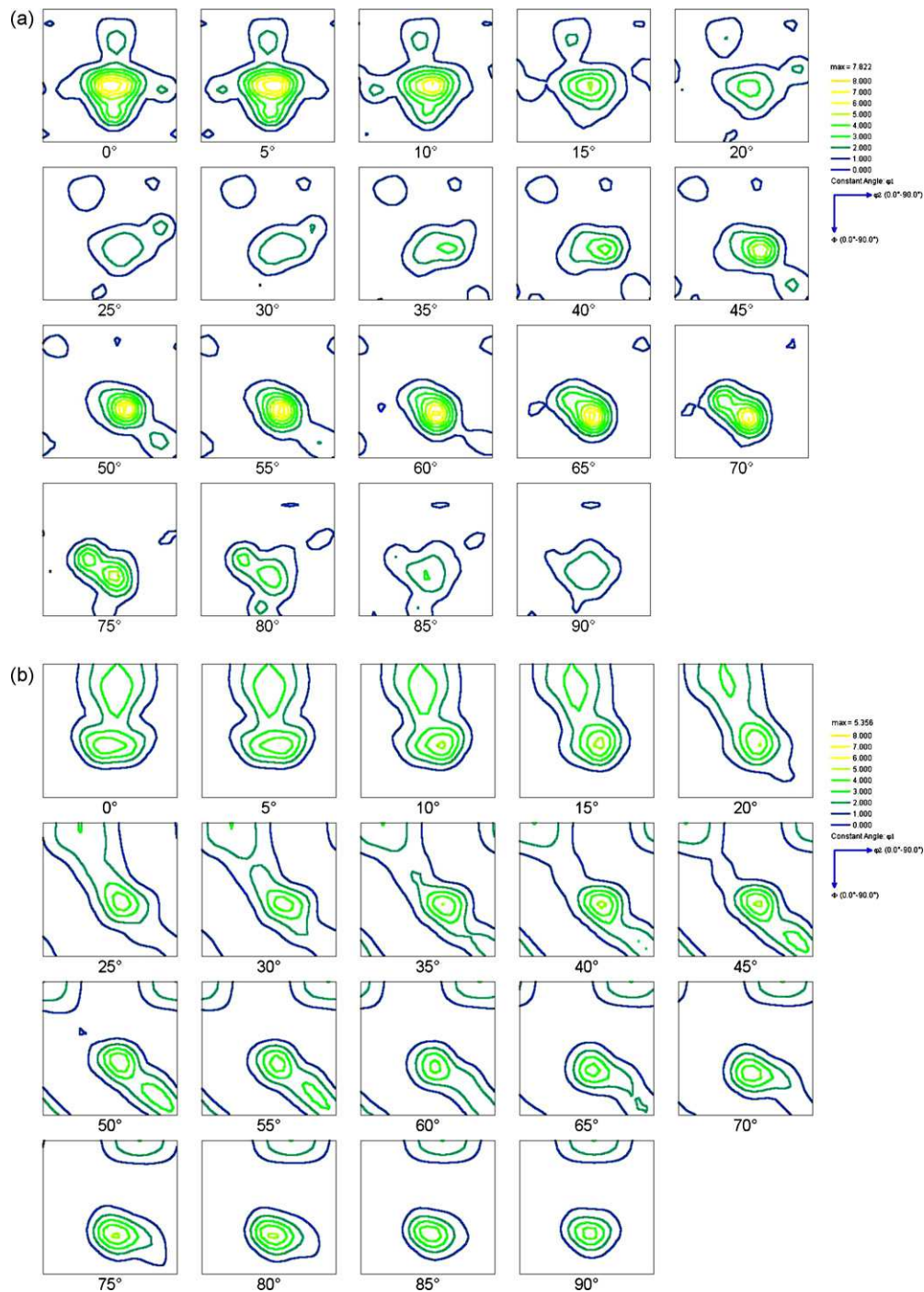


Fig. 8. (a–d) Orientation distribution functions (ODF) of 20, 50, 70 and 90% warm rolled (850 °C) samples.

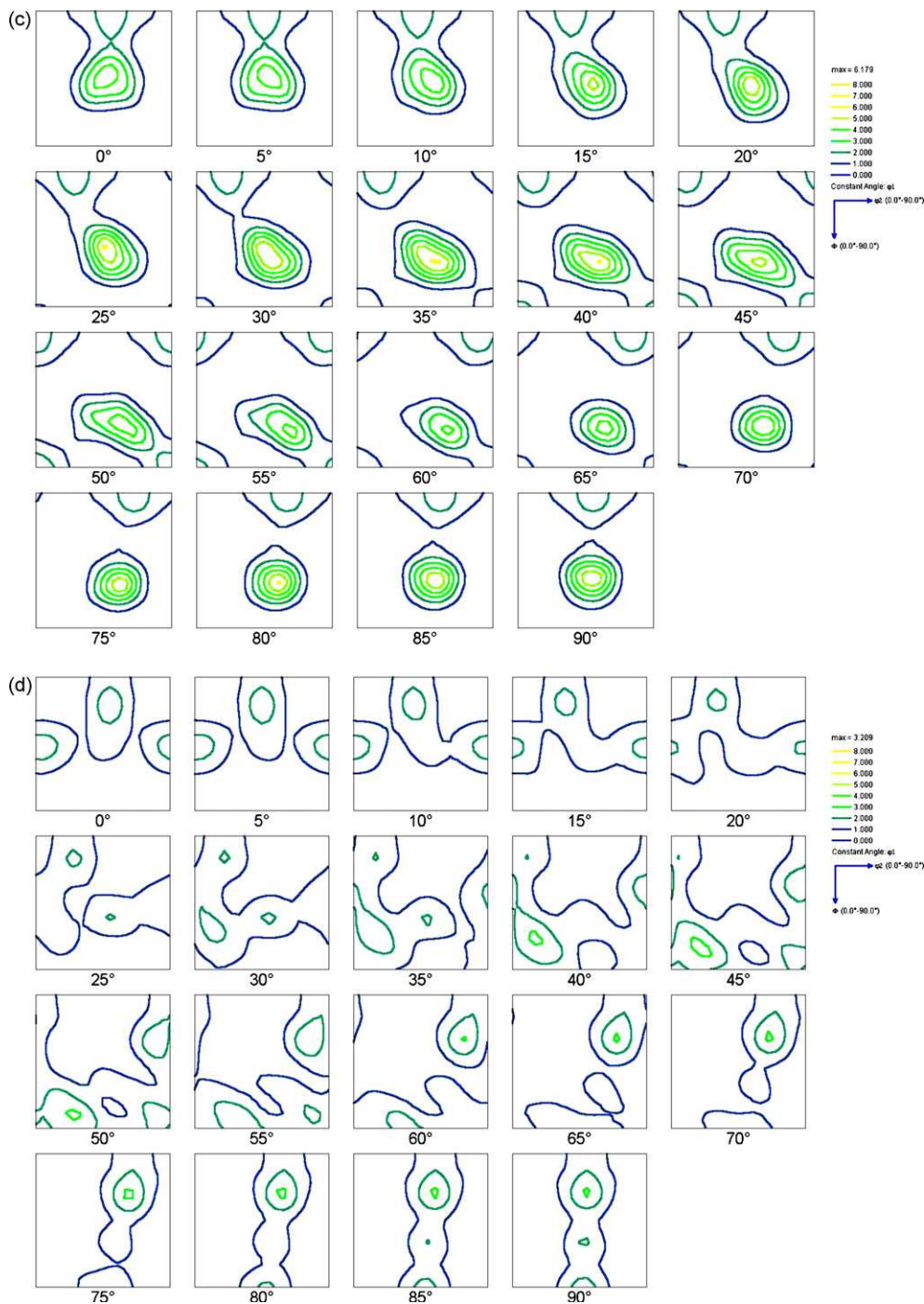


Fig. 8. (Continued).

mation texture component is rather weak after 70% rolling reduction is, therefore, primarily attributed to recrystallization. In this context the drop in the orientation density of the  $\{112\}\langle 110 \rangle$  orientation may be attributed to the favorable orientation relationship for recrystallization between the  $\{112\}\langle 110 \rangle$  deformation component and the  $\{111\}\langle 112 \rangle$  recrystallization component which is commonly observed in bcc alloys [36–41]. While partial recrystallization was observed before in other warm rolled bcc alloys at high strains (particularly when intermediate anneals were imposed between the rolling steps) a necklace-type morphology of the newly recryst-

tallized grains, as observed in the current case, is very uncommon in bcc alloys.

After 90% thickness reduction the texture and its through-thickness gradient (Figs. 7d and 8d) are quite different from the results observed after 70% thickness reduction (Figs. 7c and 8c). Two effects are particularly important. First, the material reveals a substantial gradient both, in crystallographic texture and in grain morphology. Second, particularly the outer regions of the material close to the surface are essentially recrystallized while the inner material close to the center of the sheet is mainly recovered revealing an elongated grain morphology.

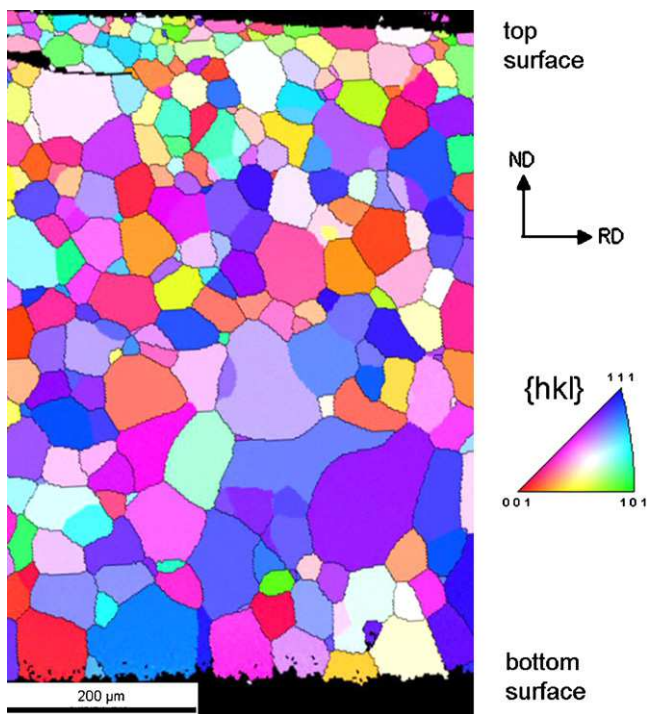


Fig. 9. EBSD  $\{hkl\}$  maps of 90% warm rolled (850 °C) and final heat treated (900 °C, 45 min) sample in longitudinal section from surface to surface.

The strong through-thickness texture and microstructure profile, which is also observed in other warm rolled alloys with bcc lattice structure, is a consequence of the macroscopic gradients in shear and temperature which occur during warm rolling [28–30,53,54].

The center layer is essentially deformed by a plane strain deformation state which promotes the formation of a strong deformation-induced  $\{001\}\langle 110\rangle$  texture component [30,37–40]. The grains in this layer typically assume an elongated pancake-type morphology in warm rolled sheets, as observed in the current case, when strong recovery prevailed. Recovery is particularly important for the preservation of some  $\alpha$ -fiber texture components, particularly of the  $\{001\}\langle 110\rangle$  orientation [33,34]. This component has a small nucleation rate for recrystallization since it typically has very weak inherited deformation-induced in-grain orientation gradients which would promote the formation of new high angle grain boundaries during nucleation [35].

As stated above, the rolling texture components in the center layer which are created essentially by a plane strain deformation state can generally be well explained in terms of Taylor-type, self-consistent or crystal plasticity finite element deformation models for bcc metals [40–51]. These models all predict the formation of a strong  $\{001\}\langle 110\rangle$  and  $\{112\}\langle 110\rangle$  texture component when assuming certain grain-scale relaxation modes, and either the 24  $\{110\}\langle 111\rangle$  plus  $\{112\}\langle 111\rangle$  or even the 48  $\{110\}\langle 111\rangle$ ,  $\{112\}\langle 111\rangle$  plus  $\{123\}\langle 111\rangle$  slip systems activated with similar critical resolved shear stress. The preservation of a strong  $\{001\}\langle 110\rangle$  texture component in conjunction with recovered pancake-shaped grains is a very typical observation in the center layer of hot rolled and cold rolled plus annealed bcc alloys [36–42].

The near-surface layers of the hot rolled sheet are characterized by a strong shear deformation and a relatively large von Mises equivalent strain. The values of the orientation densities of the shear components  $\{011\}\langle 100\rangle$  (Goss),  $\{110\}\langle 112\rangle$  and  $\{4411\}\langle 11118\rangle$  correspond to the profile of the shear strain which results from the influence of the temperature on the flow stress and the through-thickness profile of the Zener Holomon parameter [28,29,36,53,54]. Particularly the Goss orientation,  $\{011\}\langle 100\rangle$ , is well known to be stabilized by shear strain in bcc metals [28]. The strong near-surface maximum of the Goss component in hot rolled bcc metals corresponds to the ideal shear texture which is, for instance, found in torsion experiments. However, the Goss orientation,  $\{110\}\langle 001\rangle$ , is not only a strong shear texture component but it is typical of both, as-rolled and also of recrystallized grains after heavy shear deformation in bcc alloys. It is formed as a stable deformation-induced orientation in small volume fractions already during heavy shear deformation (i.e. without any contribution from recrystallization) and also as a dominant recrystallization component when these small Goss-oriented texture islands grow into the heavily strained neighboring matrix [55]. The  $\{112\}\langle 111\rangle$  orientation which is close to the ideal  $\{4411\}\langle 11118\rangle$  shear component is essentially introduced by shear deformation but not by recrystallization. Therefore, it is suggested that the strong maximum of the von Mises equivalent strain in the sub-surface layers of the warm rolled sheet promotes local shear deformation textures and recrystallization textures (instead of recovery as in the center layer). Very similar observations as in the current case have been made in the sub-surface layers of other hot rolled bcc alloys [36–42]. Particularly in highly alloyed ferritic stainless and soft magnetic FeSi steels the formation of strong shear texture components is a very typical observation [26–34].

### 5.3. Microstructure and texture after final recrystallization

After the final recrystallization anneal the microstructure is coarse grained and equiaxed. The crystallographic texture is dominated by a strong  $\{111\}\langle 112\rangle$  texture component which may be attributed to the well-known pronounced nucleation and growth of this orientation into the deformed  $\{111\}\langle uvw\rangle$  and  $\{112\}\langle 110\rangle$  oriented deformation microstructure [30,34,56–58]. Since we discussed above that in the center layer of the material the  $\{001\}\langle 110\rangle$  texture component was strongly recovered one should also consider that the texture observed in Figs. 9 and 10 result from both, recrystallization and subsequent grain growth.

Another aspect associated with the strong dominance of the  $\{111\}\langle 112\rangle$  orientation after the final recrystallization (and grain growth) heat treatment is the fact that, as observed already after 70% thickness reduction, the  $\{111\}\langle 112\rangle$  texture component was already formed as a deformation component as well as a dynamic recrystallization texture component during warm rolling. This means that the  $\{111\}\langle 112\rangle$  nuclei from the preceding dynamic recrystallization process might have served as nuclei for the subsequent static recrystallization of the  $\{111\}\langle 112\rangle$  texture during the final anneal.

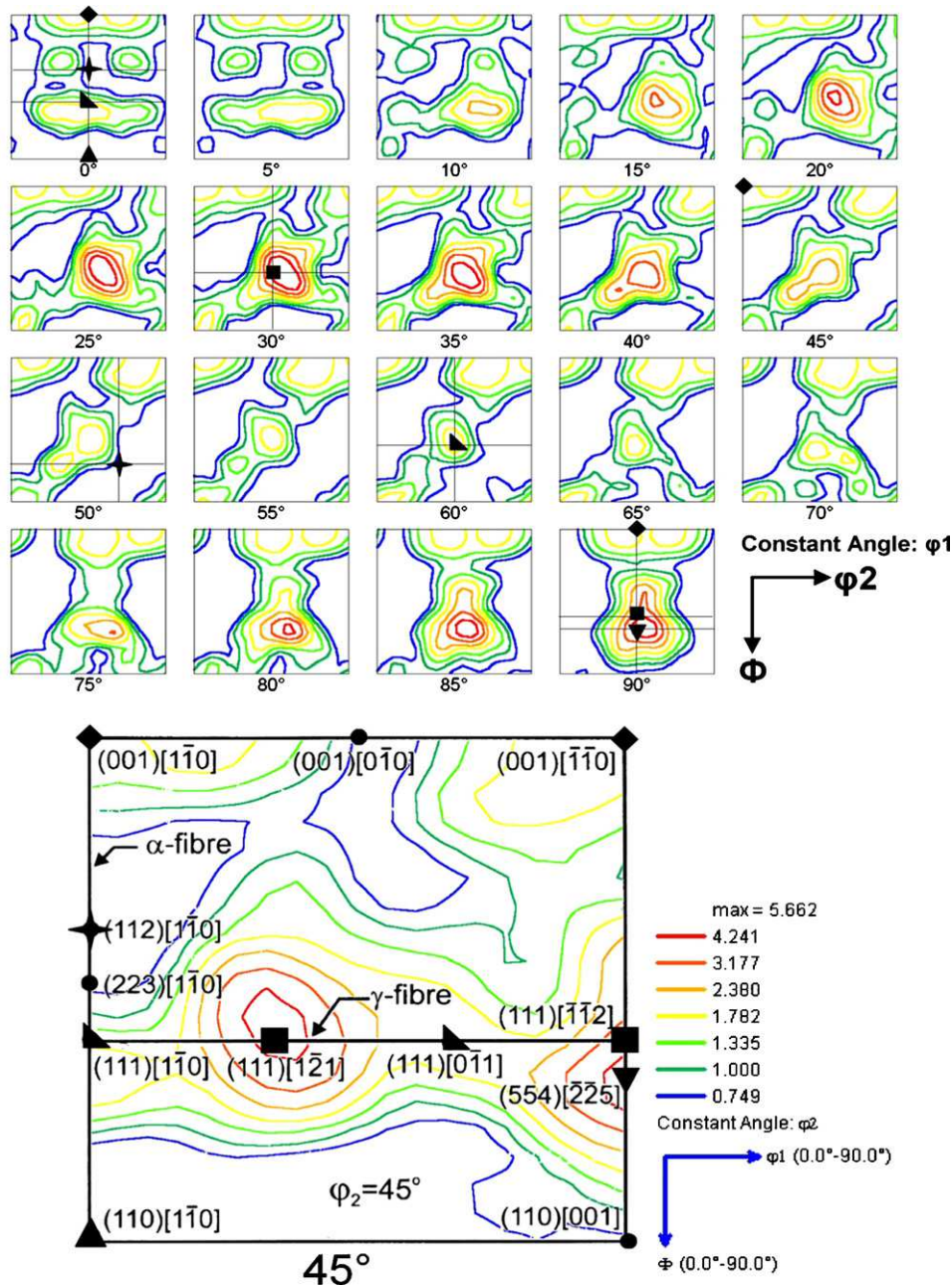


Fig. 10. Orientation distribution function (ODF) of 90% warm rolled (850 °C) and finally heat treated (900 °C, 45 min) sample.

From other bcc alloys such as Ta, Mo, Nb and ferritic steels it is known that the through-thickness microstructure and texture gradients inherited from hot rolling are often preserved to some extent after recrystallization. This applies in particular to the  $\{001\}\langle 110 \rangle$  texture in the center layers. This discrepancy to the current observation (Figs. 9 and 10), also supports the suggestion that subsequent grain growth has taken place after the recrystallization.

## 6. Conclusions

The study examined the evolution of the crystallographic texture and microstructure of a  $\beta$ -titanium alloy

(Ti–35Nb–7Zr–5Ta) during warm rolling and final recrystallization. The main conclusions are:

- At rolling reductions up to 50% the texture and microstructure evolution did not reveal pronounced gradients through the thickness. The texture evolution up to 50% was similar to other bcc alloys. Recrystallization was negligible below 50% thickness reduction.
- After 70% reduction the texture and microstructure can be explained in terms of the deformation texture components observed in other warm rolled bcc materials, and also in terms of partial recrystallization. The recrystallization process at this strain was attributed essentially to dynamic recrystallization.

- After 90% thickness reduction strong through-thickness texture and microstructure gradients were observed. These gradients were explained in terms of heavy shear at the surface and plane strain deformation in the center followed by strong dynamic and post dynamic recrystallization processes in the surface layers (top, bottom) and strong recovery in the center layer.

## References

- [1] B. de Gelas, R. Molinier, L. Seraphin, M. Armand, R. Tricot, in: J.C. Williams, A.F. Belov (Eds.), *Titanium and Titanium Alloys*, Plenum Press, New York, 1982.
- [2] D. Raabe, B. Sander, M. Friák, D. Ma, J. Neugebauer, *Acta Mater.* 55 (2007) 4475–4487.
- [3] T. Inamura, Y. Kinoshita, J.I. Kim, H.Y. Kim, H. Hosoda, K. Wakashima, S. Miyazaki, *Mater. Sci. Eng. A* 438–440 (2006) 865–869.
- [4] M. Humbert, L. Germain, N. Gey, P. Bocher, M. Jahazi, *Mater. Sci. Eng. A* 430 (2006) 157–164.
- [5] L. Germain, N. Gey, M. Humbert, P. Bocher, M. Jahazi, *Acta Mater.* 53 (2005) 3535–3543.
- [6] T. Karthikeyan, A. Dasgupta, A.J. Khan, S. Saroja, M. Vijayalakshmi, D. Bhattacharjee, V.S. Raghunathan, *Mater. Sci. Eng. A* 393 (2005) 294–302.
- [7] L. Zeng, T.R. Bieler, *Mater. Sci. Eng. A* 392 (2005) 403–414.
- [8] F. Bridier, P. Villechaise, J. Mendez, *Acta Mater.* 53 (2005) 555–567.
- [9] M.G. Glavicic, P.A. Kobryn, S.L. Semiatin, *Mater. Sci. Eng. A* 385 (2004) 372–376.
- [10] N. Stanford, P.S. Bate, *Acta Mater.* 52 (2004) 5215–5224.
- [11] M.R. Bache, *Int. J. Fatigue* 25 (2003) 1079–1087.
- [12] O.P. Karasevskaya, O.M. Ivasishin, S.L. Semiatin, Y.V. Matviychuk, *Mater. Sci. Eng. A* 354 (2003) 121–132.
- [13] M.G. Glavicic, P.A. Kobryn, T.R. Bieler, S.L. Semiatin, *Mater. Sci. Eng. A* 351 (2003) 258–264.
- [14] A.N. Kalinyuk, N.P. Trigub, V.N. Zamkov, O.M. Ivasishin, P.E. Markovsky, R.V. Teliovich, S.L. Semiatin, *Mater. Sci. Eng. A* 346 (2003) 178–188.
- [15] S. Zaeferrer, *Mater. Sci. Eng. A* 344 (2003) 20–30.
- [16] O.M. Ivasishin, S.V. Shevchenko, S.L. Semiatin, *Mater. Sci. Eng. A* 332 (2002) 343–350.
- [17] M.R. Bache, W.J. Evans, *Mater. Sci. Eng. A* 319–321 (2001) 409–414.
- [18] S.L. Semiatin, P.N. Fagin, M.G. Glavicic, I.M. Sukonnik, O.M. Ivasishin, *Mater. Sci. Eng. A* 299 (2001) 225–234.
- [19] M.R. Bache, W.J. Evans, B. Suddell, F.R.M. Herrouin, *Int. J. Fatigue* 23 (2001) 153–159.
- [20] N. Gey, M. Humbert, H. Moustahfid, *Scripta Mater.* 42 (2000) 525–530.
- [21] S. Suwas, R.K. Ray, A.K. Singh, S. Bhargava, *Acta Mater.* 47 (1999) 4585–4598.
- [22] A.K. Singh, A. Bhattacharjee, A.K. Gogia, *Mater. Sci. Eng. A* (1999) 225–230.
- [23] L. Ponsonnet, C. Quesne, R. Penelle, *Mater. Sci. Eng. A* 262 (1999) 50–63.
- [24] R.A. Lebensohn, G.R. Canova, *Acta Mater.* 45 (1997) 3687–3694.
- [25] A.W. Bowen, *Mater. Sci. Eng.* 29 (1977) 19–28.
- [26] D. Raabe, K. Lücke, *Scripta Metall.* 26 (1992) 1221–1226.
- [27] D. Raabe, *J. Mater. Sci.* 30 (1995) 47–52.
- [28] M. Hölscher, D. Raabe, K. Lücke, *Acta Metall.* 42 (1994) 879–886.
- [29] A. Fedosseev, D. Raabe, *Scripta Metall.* 30 (1994) 1–6.
- [30] D. Raabe, K. Lücke, *Mater. Sci. Technol.* 9 (1993) 302–312.
- [31] D. Raabe, *Metall. Mater. Trans. A* 26 (1995) 991–998.
- [32] D. Raabe, *Mater. Sci. Technol.* 11 (1995) 461–468.
- [33] D. Raabe, *Steel Res.* 66 (1995) 222–229.
- [34] D. Raabe, *Scripta Metall.* 33 (1995) 735–740.
- [35] D. Raabe, Z. Zhao, S.-J. Park, F. Roters, *Acta Mater.* 50 (2002) 421–440.
- [36] M. Hölscher, D. Raabe, K. Lücke, *Steel Res.* 62 (1991) 567–575.
- [37] D. Raabe, K. Lücke, G. Gottstein, *J. de Phys. IV, Colloque C7, Supplé. J. de Phys. III 3* (1993) 523–526.
- [38] D. Raabe, B. Mülders, K. Lücke, G. Gottstein, *Mater. Sci. Forum* 157–162 (1994) 841–846.
- [39] D. Raabe, G. Schlenkert, H. Weisshaupt, K. Lücke, *Mater. Sci. Technol.* 10 (1994) 229–305.
- [40] D. Raabe, K. Lücke, *Z. Metallk* 85 (1994) 302–306.
- [41] D. Raabe, J. Ball, G. Gottstein, *Scripta Metall.* 27 (1992) 211–216.
- [42] I. Thomas, S. Zaeferrer, F. Friedel, D. Raabe, *Adv. Eng. Mater.* 5 (2003) 566–570.
- [43] E. Aernoudt, P. Van Houtte, T. Leffers, in: H. Mughrabi (Ed.), *Mater. Sci. Technol.*, vol. 6, in: R.W. Cahn, P. Haasen, E.J. Kramer (Eds.), VCH, 1993, p. 89.
- [44] J.L. Raphanel, P. Van Houtte, *Acta Metall.* 33 (1985) 1481–1492.
- [45] L. Tóth, A. Molinari, D. Raabe, *Metall. Trans. A* 28A (1997) 2343–2351.
- [46] P. Van Houtte, L. Delannay, I. Samajdar, *Text. Microstruct.* 31 (1999) 109–149.
- [47] B. Peeters, M. Seefeldt, P. Van Houtte, E. Aernoudt, *Scripta Mater.* 45 (2001) 1349–1356.
- [48] U.F. Kocks, C.N. Tomé, H.-R. Wenk, *Texture and Anisotropy. Preferred Orientations in Polycrystals and their Effect on Material Properties*, Cambridge University Press, Cambridge, UK, 1998.
- [49] D. Raabe, *Mater. Sci. Eng. A* 197 (1995) 31–37.
- [50] D. Raabe, *Mater. Sci. Technol.* 11 (1995) 455–460.
- [51] F. Roters, H.S. Jeon-Haurand, D. Raabe, *Mater. Sci. Forum* 495–497 (2005) 937–944.
- [52] D. Raabe, W. Mao, *Philos. Mag. A* 71 (1995) 805–813.
- [53] J.H. Beynon, A.R.S. Ponter, C.M. Sellars, *Process. Model. of Met. Forming*, vol. 321, Kluwer Academic Publishers, 1988.
- [54] A.J. McLaren, C.M. Sellars, in: N.D. Ryan, A.J. Brown, H.J. McQueen (Eds.), *Proc. Int. Conf. on Strip Cast., Hot a. Cold Working of Stainl. Steels*, vol. 107, The Metall. Soc. of CIM, Quebec, Canada, 1993.
- [55] N. Chen, S. Zaeferrer, L. Lahn, K. Günther, D. Raabe, *Acta Mater.* 51 (2003) 1755–1765.
- [56] W.B. Hutchinson, *Int. Mater. Rev.* 29 (1984) 25–37.
- [57] K. Ushioda, W.B. Hutchinson, J. Agren, U. von Schlippenbach, *Mater. Sci. Technol.* 2 (1986) 807–815.
- [58] W.B. Hutchinson, *Acta Metall.* 37 (1989) 1047–1056.